# Stability and Physical Properties of Metastable Ba–Si Clathrates

Romain Viennois, Régis Debord, Adrien Moll, Vincent Legrand, Mickaël Beaudhuin, Nicole Fréty, Stéphane Pailhès

# Stability and physical properties of metastable Ba-Si clathrates

Romain Viennois[1,*], Régis Debord[2], Adrien Moll[1], Vincent Legrand[1], Mickaël Beaudhuin[1], Nicole Fréty[1,*], Stéphane Pailhès[2,*]

[1]ICGM, Univ Montpellier, CNRS, ENSCM, Montpellier, France

[2]Institut Lumière Matière, UMR5306 Université Lyon 1-CNRS, Université de Lyon 69622 Villeurbanne cedex, France

[*] *Corresponding authors: romain.viennois@umontpellier.fr; nicole.frety@umontpellier.fr ;*

*stephane.pailhes@univ-lyon1.fr*

## Abstract

In the present paper, we have investigated the stability of different Ba-Si clathrates with pressure and temperature using DFT calculations and studied the stability of type I $Ba_8Si_{46}$ and type IX $Ba_{24}Si_{100}$ clathrates using high pressure – high temperature synthesis technique, calorimetry and diffraction experiments. When increasing pressure, the type I $Ba_8Si_{46}$ clathrate and $BaSi_6$ become more stable. In good qualitative agreement with experiments, the type IX $Ba_{24}Si_{100}$ clathrate becomes stable at pressure of 1-2 GPa thanks to pressure and thermal effect of both electronic and vibrational contributions. One can notice that the presence of Ba in the cages of type IX clathrate increases significantly the stability and the mechanical properties of type IX clathrate. We have determined the P-T existence domain of type IX $Ba_{24}Si_{100}$ clathrate from ex-situ experiments, which was confirmed by in-situ synchrotron X-ray experiments. At room pressure and under oxidizing atmosphere, the type I $Ba_8Si_{46}$ and the type IX $Ba_{24}Si_{100}$ clathrates are stable up to about 560°C and up to about 600°C, respectively. The thermoelectric properties of type IX $Ba_{24}Si_{100}$ are also reported.

**Key words**

Clathrates, pressure, stability, DFT, in-situ experiments, thermoelectricity

## 1. Introduction

Clathrates are a family of host-guest compounds with a covalent lattice composed of face-sharing polyhedral cages in which are intercalated loosely bonded atoms or molecules [1-3]. The clathrate structures were firstly discovered in 1951 for gas hydrate compounds [4-6] and later on for silicates [7] and Si intermetallics [1,8]. These clathrate structures are formed of cage framework made of water, silica or silicon and within these cages, gas species can be intercalated in hydrate and silicate clathrates or alkaline metal in silicon clathrates. In the case of hydrate clathrates, depending on the intercalated species in the cages, many different clathrate structures exist whereas only type I and type II inorganic clathrate cubic structures with respectively $M_8X_{46}$ and $M_6X_{34}$ chemical formula (with M = alkaline metal, and X = Si, Ge, Sn) were found at this time [1]. However, more recently, other M intercalated atoms such as alkaline earth, halogen or even some rare-earth were found, thanks to the use of out-of-equilibrium techniques such as high pressure – high temperature synthesis techniques [1]. Since two decades, several new clathrate structures were discovered for the intermetallic clathrates. When substituting 16 X atoms of column 14 by 16 Y atoms of column 13 in $M_8X_{46}$, a new cubic clathrate structure containing only one type of cage and of $M_8Y_{16}X_{30}$ chemical formula was discovered: the type VIII clathrate [2,3,9]. Another cubic crystal structure can be derived from type I clathrate: the type IX clathrate with $M_{24}X_{100}$ chemical formula [10-16]. When using pressure larger than 5 GPa in high pressure – high temperature synthesis technique, a new orthorhombic structure made of tunnels and derived from $EuGa_2Ge_4$ [17] was discovered and has $MX_6$ chemical formula [16,18]. Type III tetragonal intermetallic clathrate was also found for two cases [1,2]. Defects play also an important role in determining the structure of clathrates, superstructures were observed and ascribed to correlated vacancies on the framework structure [2,3,10]. More recently, a surprising collective dynamics of point defects has been identified as the mechanism of an isostructural transition at high pressure [19]. Thanks to the richness of their structural

complexity, clathrates are materials that can be engineered at the scale of their unit cell for use in various applications and present a wide panels of interesting properties [1-3,16,18-21] as for example: superconductivity, n- and p-type semiconducting properties, good thermoelectric properties, good optical properties, good mechanical properties, etc.

Among clathrates, Ba-Si clathrates are metastable and can be synthesized using high pressure - high temperature technique [16,18-22]. There exist three different clathrate compounds [16,18-24]: $Ba_{24}Si_{100}$ which can be synthesized around 1 GPa and is superconducting below 1.55 K; $Ba_8Si_{46}$ which can be synthesized above 1.5 GPa and is superconducting below 8 K; $BaSi_6$ which can be obtained at 10 GPa. However, the existence domain in the (P, T) range has been studied only for the type 1 clathrate $Ba_{8-x}Si_{46}$ [21,25,26] and not in the case of $Ba_{24}Si_{100}$. Moreover, if Castillo et al [27] reported the decomposition of the type 1 clathrate $Ba_{8-x}Si_{46}$ at 611°C under inert atmosphere, it was not studied under air and neither the reaction process nor the stability of $Ba_{24}Si_{100}$ has been studied under room pressure. $Ba_{8-x}Si_{46}$ can also be obtained using redox reactions [28]. Recently, we have shown the possibility to obtain high amount of $Ba_{24}Si_{100}$ by mechanical alloying with low amount of secondary phases [29]. The aim of the present work is to fulfill the knowledge of the (P, T) existence domain and to study the stability of $Ba_8Si_{46}$ and $Ba_{24}Si_{100}$.

In this paper, we focus on the stability of binary metastable Ba-Si clathrates by a combined theoretical and experimental study and more particularly in the case of $Ba_{24}Si_{100}$ which is also studied using in-situ techniques and whose thermoelectric properties are reported.


## 2. Computation and experimental details

The DFT calculations were based on PAW pseudopotentials and the PBE exchange-correlation functional using the Vienna *ab initio* Simulation Package (VASP) [30,31]. For all calculations an energy cut-off of 350 eV was applied and the force convergence was $10^{-3}$ eV/Å and the energy convergence was $10^{-10}$ eV. We applied k-meshes of 5x5x5 for $Ba_{24}Si_{100}$ and $Si_{100}$, of 9x9x9 for type I and VIII $Ba_8Si_{46}$ and $Si_{46}$, for type II $Ba_6Si_{34}$ and $Si_{34}$ and of 16x16x8 for $Ba_4Si_{24}$ and $Si_{24}$. In order to determine the equation of states of the different compounds, series of calculations of the energy have been performed

for different fixed volumes while keeping the shape of the cell and the atomic positions free to relax. Otherwise, the calculation conditions are the same as for the structure relaxation. In order to determine the bulk modulus and its pressure derivative, we have used the Birch-Murnaghan equation to fit the equation $E = f(V)$ [32]. The formation enthalpy $H_{form}$ of $Ba_xSi_y$ compounds has been calculated as following:

$$H_{form}(Ba_xSi_y) = (E(Ba_xSi_y)-xE(Ba)-yE(Si))/(x+y) \qquad (1)$$

where $E(Ba_xSi_y)$ is the energy of the compound $Ba_xSi_y$, $E(Ba)$ and $E(Si)$ are the energy per atom of elemental Ba and Si. The reaction enthalpy $H_{react}$ is the energy for the reaction $x\ BaSi_2 + (y-2x)\ Si \Rightarrow Ba_xSi_y$ and is as following:

$$H_{react}(Ba_xSi_y) = H_{form}(Ba_xSi_y) - (x/x+y)H_{form}(BaSi_2) - ((y-2x)/x+y)H_{form}(Si) \qquad (2)$$

where $H_{form}(BaSi_2)$ is the formation enthalpy of $BaSi_2$ and $H_{form}(Si)$ is the formation enthalpy of silicon. When the calculations are performed under high pressure and high temperature, we take into account to the PV term and we calculate the Gibbs energy $G(P,T)$ as following [33]:

$$G(P,T) = E(V) + PV + F_{vib}(T) + F_{el}(T) = H\ (V,P) + F_{vib}(T) + F_{el}(T) \qquad (3)$$

where $H\ (V,P)$ is the enthalpy, $F_{vib}(T)$ is the vibrational free energy and $F_{el}(T)$ is the electronic free energy. In the present calculations, we have not determined the effect of the thermal expansion to the enthalpy and Gibbs energy notably on the PV term in the equation (3) as it is beyond the scope of the present work. This would necessitate the calculations of the thermal expansion of the different clathrate compounds, as well as of the $BaSi_2$ compounds and of the Ba and Si references, which is also beyond the scope of the present work. However, we must note that the Ba-Si clathrate compounds have larger linear thermal expansion (10-12 $MK^{-1}$ at room temperature) [24] than diamond Si (2.6 $MK^{-1}$ at room temperature) [34] but smaller than Ba metal (20.6 $MK^{-1}$ at room temperature) [35]. As the clathrates are Si-rich compounds, we expect a larger PV contribution and therefore a larger formation Gibbs energy $G_{form}(P,T)$ of the clathrate compounds. On the other hand, the orthorhombic $BaSi_2$ have also a larger thermal expansion (15.9 $MK^{-1}$ at room temperature) [34] than the clathrates and it is therefore difficult to determine the impact of the thermal expansion on PV for the calculation of the reaction Gibbs energy

$G_{react}(P,T)$ of the clathrate. Nevertheless, this should slightly change the temperature at which the clathrate can be formed.

We have calculated the energy for the high pressure phases of Si, Ba and $BaSi_2$ which become stable at high pressures. At room pressure, $BaSi_2$ crystallizes in an orthorhombic structure, whereas it crystallizes in the same cubic structure than $SrSi_2$ between 1-1.5 GPa and 6 GPa and between 550°C and 850-900°C, and it crystallizes in the same trigonal structure than $EuGe_2$ between 1-1.5 GPa and 6 GPa and between 400°C and 550°C and above 6 GPa [36,37]. At 0 and 1.5 GPa, we have calculated the lattice dynamics properties of bcc Ba, diamond Si, orthorhombic $BaSi_2$, cubic $BaSi_2$, trigonal $BaSi_2$, $Ba_{24}Si_{100}$, $Ba_8Si_{46}$ and $Ba_4Si_{24}$. From these calculations, we have calculated the vibrational free energy $F_{vib}$ in function of the temperature. From the electronic density of states, we have calculated the electronic free energy $F_{el}$ using the Sommerfeld model as done by Colinet et al for ZrSi [33]. Thus, the calculations of the Gibbs energy in function of the temperature take into account both the vibrational and electronic contributions. We have performed high pressure and high temperature synthesis of type IX $Ba_{24}Si_{100}$ using a belt apparatus that can reach 5 GPa and 1100°C inside a boron nitride crucible within a graphite furnace that hold the mixture. It was also possible to make high pressure and high temperature synthesis of type IX $Ba_{24}Si_{100}$ using a piston cylinder apparatus reaching 5 GPa and 1200 °C. We use stoichiometric amount of powders of orthorhombic $BaSi_2$ (Cerac, 98.%) and Si (Sigma Aldrich, 99.999%) for high pressure and high temperature synthesis. The mixture was submitted to a pressure in the range 0.2-1.8 GPa followed by heating in a [575-850]°C temperature range during one hour in the case of $Ba_{24}Si_{100}$ and to a pressure of about 3 GPa followed by heating to 800°C during one hour in the case of $Ba_8Si_{46}$. The samples were then thermally quenched and the pressure was slowly decreased. More details can be found in refs. 21 and 22. We then characterize their phase constitution with X-ray diffraction on a DB8 diffractometer using Bragg Brentano configuration. The data were analyzed by Rietveld refinement using the GSAS software.

The in-situ X-ray diffraction experiments were performed on the ID27 beamline at the ESRF with a Paris Edinburg press allowing a sample dimension of 5 mm in diameter and in height. The boron nitride was used as pressure transmitting medium. The sample was encapsulated in a h-BN crucible in order to

electrically isolate it from the graphite furnace that provides the high temperature. The pressure was measured via the cell parameters of gold and h-BN. The temperature was measured with a thermocouple (K type) placed through the boron epoxy gasket inside the sample environment. The pressure was adjusted during heating to be maintained at 1.0 GPa. The wavelength used was 0.202150 Å. The data were analyzed by Rietveld refinement using the GSAS software [38].

The thermal stability was studied from simultaneously differential thermal analysis (DTA) and thermogravimetric analysis (TGA) using a Setaram equipment (Labsys) with alumina crucibles. DTA/TGA experiments were performed from room temperature to 1000°C in Ar or air atmospheres with a heating rate of 5°C/min and natural cooling to room temperature. Note that the DTA/TGA experiments under Ar and under air have been performed on two different $Ba_{24}Si_{100}$ samples whereas on the same batch of sample for $Ba_8Si_{46}$. Powders were analyzed using X-ray diffraction (Philips X'PERT, Cu-$K_\alpha$ radiation with an accelerated detector PW 3050/60 at 45 kV, 30 mA settings). The crystalline structure and phase purity were analyzed by Rietveld refinement of the XRD patterns with Fullprof software [39]. The electrical resistivity, $\rho$, was measured with a homemade apparatus in the van der Pauw configuration with four tungsten tips under vacuum between room temperature and 400°C. The Seebeck coefficient, $\alpha$, was also measured with two different homemade apparatus at low temperature and at high temperature. The sample was heated under vacuum on one side with high power light in order to obtain a temperature gradient of about 5°C across the sample and both the temperature and voltage are measured on each face of the sample with chromel and alumel thermocouples. The Seebeck coefficient and electrical resistivity measurements were made on a 5mm diameter and 2mm thick pellet.

## 3. Computation results

We have performed the structure relaxation of the different existing metastable Ba-Si clathrate phases namely the type IX cubic $Ba_{24}Si_{100}$, the type I cubic $Ba_8Si_{46}$, the orthorhombic $BaSi_6$, as well as the fictitious type II $Ba_6Si_{34}$ and type VIII $Ba_8Si_{46}$. We have also performed the structure relaxation of the corresponding empty clathrate phases. For comparison and to enable the evaluation of the stability of

these phases, we have performed the calculations of diamond Si and orthorhombic $BaSi_2$ phases, which are the stable Si rich binary Ba-Si phases. The lattice parameters of these different phases are reported in Tables 1, 2 and 3 together with the experimental values when they are available [40-46] (see the supplementary information for the detailed computed structures). The DFT calculations overestimate the lattice parameters as this is usually the case for the GGA exchange-correlation functional. The formation enthalpy $H_{form}$ of these different compounds at P = 0 GPa are reported in Figure 1-a. One can see that all the Si-rich compounds are less stable than a mixture of Si and $BaSi_2$. One can determine the reaction energies for the formation of these compounds from a mixture of Si and $BaSi_2$ and this is reported at P = 0 GPa in the Figure 2-a.

| Compounds | a (Å) | $V_{at}$ (Å$^3$) | $H_{form}$ (eV/at) | B (GPa) | dB/dP | |
|---|---|---|---|---|---|---|
| Diamond Si | 5.4686 | 20.442 | | 89 | 4.5 | This work |
| | 5.4309 | 20.023 | | 97.88 | 4.24 | Exp. [40] |
| Type 1 Si$_{46}$ | 10.2275 | 23.257 | 0.0628 | 76 | 4.75 | This work |
| Type II Si$_{34}$ | 14.7387 | 23.542 | 0.0523 | 76.2 | 4.7 | This work |
| | 14.626 | 23.006 | | 90 | 5.2 | Exp. [40-42] |
| Type VIII Si$_{23}$ | 10.101 | 22.403 | 0.0816 | 79.5 | 4.75 | This work |
| Type IX Si$_{100}$ | 14.206 | 28.669 | 0.3835 | 37.7 | 4.15 | This work |

**Table 1**: Lattice parameters, atomic volume $V_{at}$, formation enthalpies $H_{form}$, bulk modulus B and its pressure derivative dB/dP of diamond Si and empty Si clathrates.

| Compounds | a (Å) | $V_{at}$ (Å$^3$) | $H_{form}$ (eV/at) | B (GPa) | dB/dP | |
|---|---|---|---|---|---|---|
| Type 1 Ba$_8$Si$_{46}$ | 10.3946 | 20.798 | -0.1072 | 72.5 | 5.75 | This work |
| Type 1 Ba$_{7.76}$Si$_{46}$ | 10.3141 | 20.41 | | 93 | | Exp. [43,44] |
| Type 1 Ba$_6$Si$_{46}$ | 10.3066 | 21.054 | -0.0864 | 76 | 5.6 | This work |
| Type 1 Ba$_{6.63}$Si$_{46}$ | 10.2652 | 20.553 | | | | [41] |
| Type II Ba$_6$Si$_{34}$ | 15.0066 | 21.121 | -0.0834 | 72.5 | 5.75 | This work |
| Type VIII Ba$_4$Si$_{23}$ | 10.3831 | 20.729 | -0.0358 | 68.2 | 6.2 | This work |
| Type IX Ba$_{24}$Si$_{100}$ | 14.164 | 22.916 | -0.1845 | 58.7 | 4.7 | This work |
| | 14.0685 | 22.455 | | 64.9 | 3.75 | Exp. [15,45] |

**Table 2**: Lattice parameters, atomic volume $V_{at}$, formation enthalpies $H_{form}$, bulk modulus B and its pressure derivative dB/dP of Ba-Si clathrates.

| Compounds | a (Å) | b (Å) | c (Å) | $V_{at}$ (Å$^3$) | $H_{form}$ (eV/at) | B (GPa) | dB/dP | |
|---|---|---|---|---|---|---|---|---|
| Si$_{24}$ | 3.8504 | 10.7466 | 12.7443 | 21.972 | 0.0903 | 76.5 | 4.8 | |
| | 3.82 | 10.7 | 12.63 | 21.51 | | 86-91 | 5.4-8 | Exp. [18,46] |
| Ba$_4$Si$_{24}$ | 4.5089 | 10.4212 | 12.0476 | 20.217 | -0.0814 | 70.2 | 5.25 | |
| | 4.485 | 10.375 | 11.969 | 19.891 | | | | Exp. [16] |

**Table 3**: Lattice parameters, atomic volume $V_{at}$, formation enthalpies $H_{form}$, bulk modulus B and its pressure derivative dB/dP of orthorhombic Si$_{24}$ and Ba$_4$Si$_{24}$.
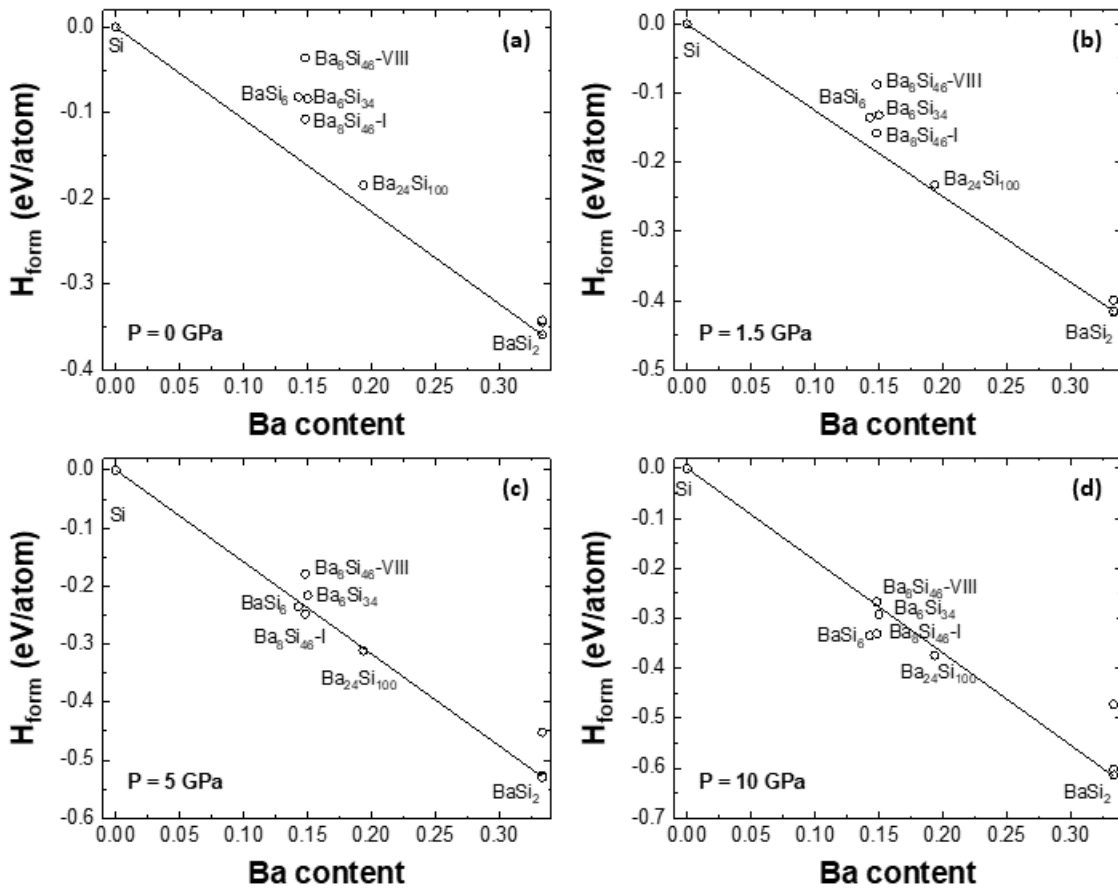


**Figure 1:** Formation enthalpies $H_{form}$ of the different Ba-Si phases as function of the Ba content at 0 GPa (a), 1.5 GPa (b), 5 GPa (c) and 10 GPa (d).

It shows that rather low reaction energy is needed for the formation of these compounds. As reported in a previous paper, type IX Ba$_{24}$Si$_{100}$ has the lowest $E_{reaction}$ and this compound can form under high

pressure-high temperature conditions with rather low pressure [15,22,23] or by mechanical alloying [29]. Type I $Ba_8Si_{46}$ and $Ba_4Si_{24}$ (or $BaSi_6$) have respectively the next two lower values of the reaction energies. These compositions have been synthesized under high pressure-high temperature conditions [16,20,21]. Interestingly, type II $Ba_6Si_{34}$ has only slightly larger reaction energy and has never been observed so far. On the other hand, type VIII $Ba_8Si_{46}$ has a high reaction energy and shouldn't be accessible. It questions the stability of the type VIII $M_8Si_{46}$ clathrates, which have been previously studied using DFT calculations but without consideration of their stabilities [47].
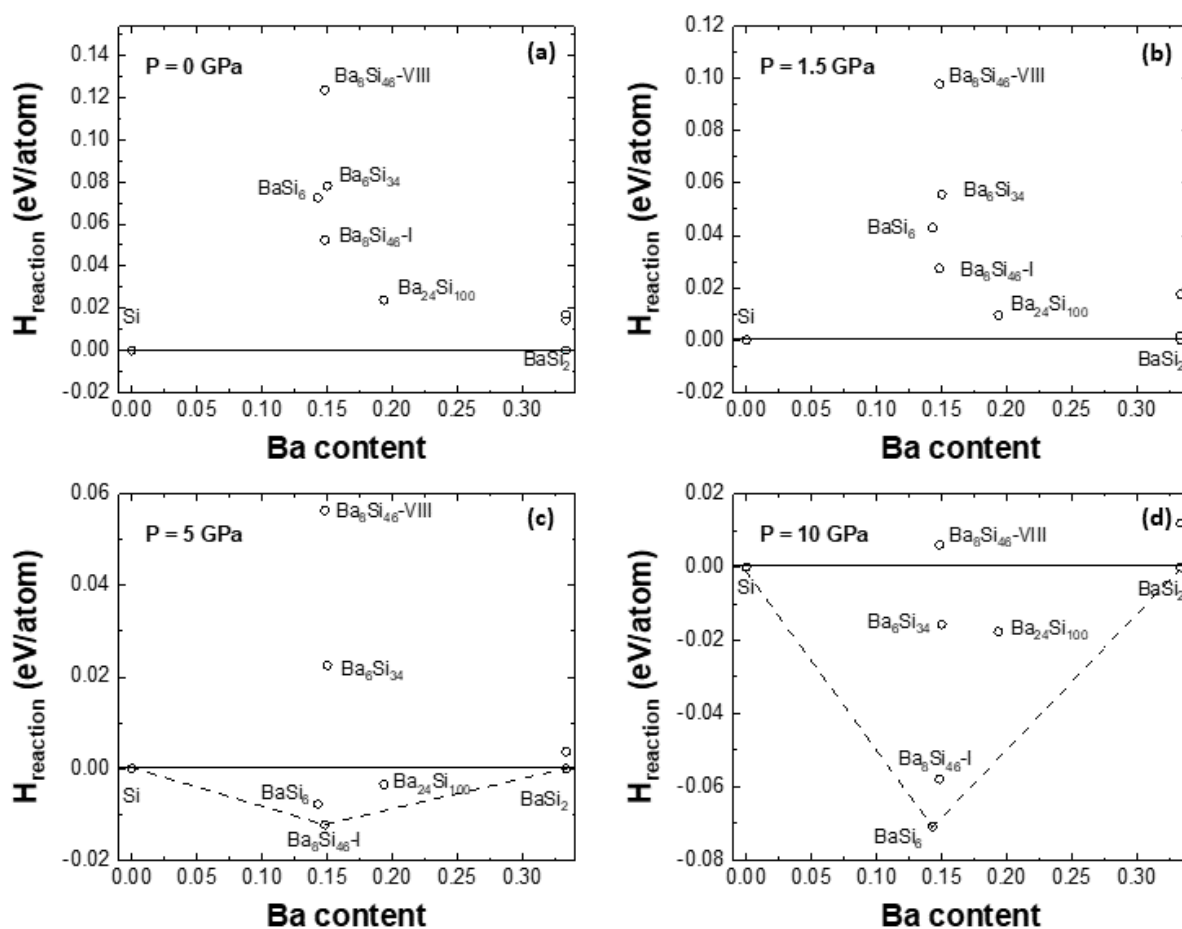


**Figure 2:** Reaction enthalpies $H_{react}$ of the different Ba-Si phases versus x $BaSi_2$ + y Si as function of the Ba content at 0 GPa (a), 1.5 GPa (b), 5 GPa (c) and 10 GPa (d).

When comparing the formation energies of the different empty clathrate phases with that of diamond silicon (see Table 1 and supplementary information), one can see that the type I $Si_{46}$ and the type II $Si_{34}$ are the most stable phases, that $Si_{24}$ and type VIII $Si_{46}$ are less stable with similar formation energy and

that type IX $Si_{100}$ is unstable and very expanded phase with $H_{form}$ as high as 0.385 eV/at. This is higher than the formation energies of the 114 Si allotropes predicted by Amsler et al [48]. However, the Ba-filled cage structure of type IX clathrate becomes the most stable rich-Si Ba-Si phase (see Table 1 and 2, and Figure 1a). Contrary to the other open framework structures studied here, the volume of the cell decreased with the intercalation of the barium atoms in the cages. This means that the bondings between the guest atoms and the framework silicon atoms are strongly attractive and that the presence of the guest atoms is fundamental for the stability of the type IX clathrate structure. Our results confirm that even if an open framework structure is strongly unfavorable energetically when empty, it can be strongly stabilized when guest atoms are intercalated, calling for systematic study of the different structures found by Amsler et al [48] with different guest atom intercalation, as this has been done more recently for type I clathrate [49].

We have investigated the effect of pressure on the stability of the different cage structures stabilized under HP-HT conditions in the experiments. We report the formation energies and the reaction energies of the different Clathrate phases at several pressures in the Figures 1 and 2. One can see that at 1.5 GPa, the most stable structure is type IX $Ba_{24}Si_{100}$ which has slightly positive $H_{reac}$, whereas the most stable structures at 5 GPa and 10 GPa are the type I $Ba_8Si_{46}$ and $Ba_4Si_{24}$, respectively, with both negative $H_{react}$. At all pressure, the less stable compounds are the type VIII $Ba_8Si_{46}$ followed by the type II $Ba_6Si_{34}$. We report the reaction enthalpy $H_{react}$ of type IX $Ba_{24}Si_{100}$, type I $Ba_8Si_{46}$ and $Ba_4Si_{24}$ as function of the pressure in the Figure 3. $Ba_{24}Si_{100}$ is the most stable structure until 3.85 GPa although it is still metastable. Above 3.85 GPa, both $Ba_{24}Si_{100}$ and type I $Ba_8Si_{46}$ become more stable than the mixture of Si and $BaSi_2$ but only type I $Ba_8Si_{46}$ is stable. Above 6.3 GPa, $Ba_4Si_{24}$ become the most stable structure.

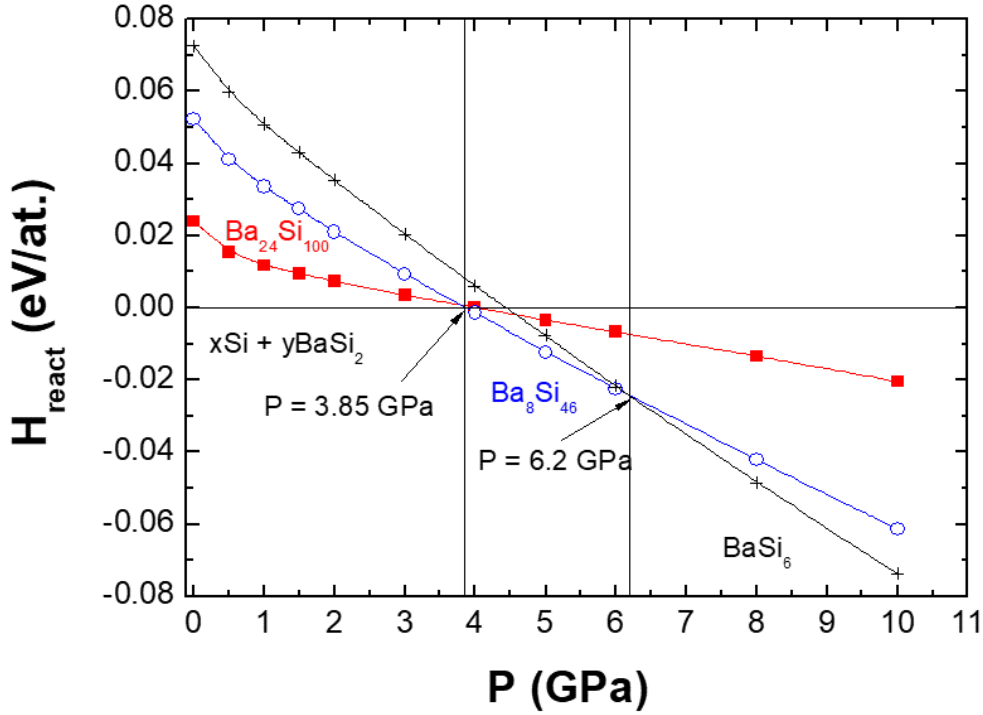**Figure 3:** Reaction enthalpies $H_{react}$ of type IX $Ba_{24}Si_{100}$,(red filled squares) type I $Ba_8Si_{46}$ (blue open circles) and $Ba_4Si_{24}$ (black stars) as function of the pressure.

Our results concerning type I $Ba_8Si_{46}$ and $Ba_4Si_{24}$ agree with the experimental results [16] and with prior calculations [50]. But $Ba_{24}Si_{100}$ is never more stable than the mixture of Si and $BaSi_2$ or than $Ba_8Si_{46}$. However, the calculations in the Figure 3 are done at 0 K. We have calculated the reaction Gibbs energies of the three different phases as function of the temperature at 0 and 1.5 GPa (see Figure. 4). We see that at 1.5 GPa $Ba_{24}Si_{100}$ becomes more stable than the mixture of Si and $BaSi_2$ above 385°C and $Ba_8Si_{46}$ becomes more stable above 997 °C. This means that these phases are metastable HP-HT phases that could be stabilized by temperature quenching, as it is observed experimentally [15,16,20-23]. On the other hand, $BaSi_6$ remains unstable over the overall temperature range at 0 and 1.5 GPa. Note that the kink observed at 582°C on the $Ba_{24}Si_{100}$ curve is not an artefact in the Figure 4 (b) but is related to the structural transition from cubic to orthorhombic $BaSi_2$, as observed experimentally by Evers [36]. Indeed, as can be seen in the figure S2 of the supplementary information, the formation Gibbs energy $G_{form}$ of $BaSi_2$ at P = 1.5 GPa becomes lower in the orthorhombic phase than in the cubic phase above 582°C. Therefore, the reaction Gibbs energy $G_{react}$ of the clathrate phases are determined using the

11

formation Gibbs energy $G_{form}$ of the cubic $BaSi_2$ below 582°C and using the formation Gibbs energy $G_{form}$ of the orthorhombic $BaSi_2$ phase above 582°C. We note that the $G_{react}$ decreases more slowly with the temperature when orthorhombic $BaSi_2$ becomes the most stable $BaSi_2$ phase. Our calculations show that both the vibrational and electronic thermal contributions are necessary for stabilizing $Ba_{24}Si_{100}$ and $Ba_8Si_{46}$ at 1.5 GPa. $Ba_8Si_{46}$ becomes more stable than $Ba_{24}Si_{100}$ either by increasing the temperature at 1.5 GPa or by increasing the pressure up to 3.85 GPa at 0 K. As we will see below, this qualitatively agrees with the experiments.
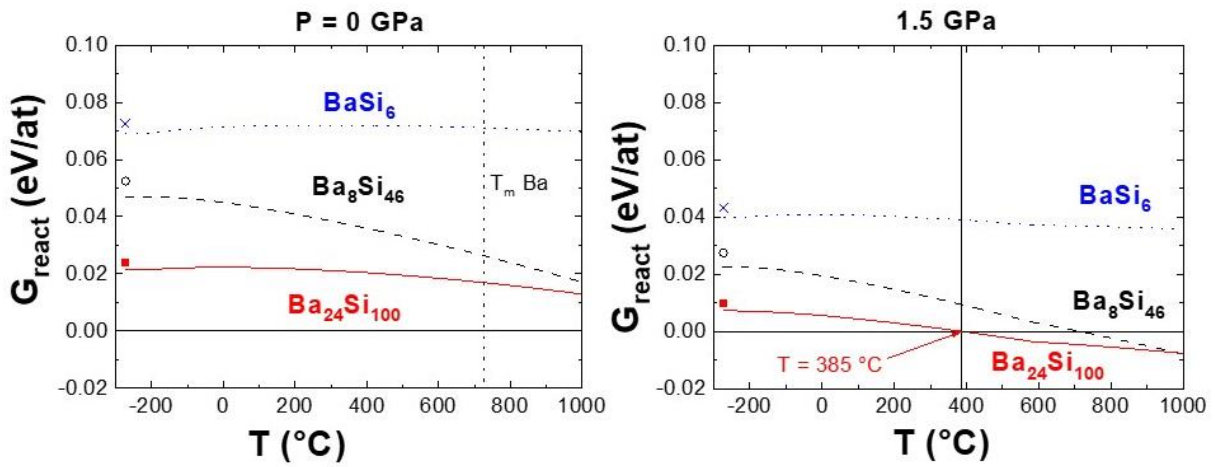


**Figure 4:** Reaction Gibbs energies $G_{react}$ of type IX $Ba_{24}Si_{100}$, type I $Ba_8Si_{46}$ and $Ba_4Si_{24}$ as function of the temperature at 0 and 1.5 GPa. The symbols correspond to the 0 K values without the vibrational contribution.

We have also considered the case of defected type I $Ba_8Si_{46}$ and type IX $Ba_{24}Si_{100}$ clathrates. We have studied the case of Si and Ba vacancies, reported in Tables 4 and 5. When comparing the evolution of the reaction enthalpy $H_{react}$, one can see that vacancies are promoted only in the case of the site Ba1 of $Ba_8Si_{46}$ which corresponds to the (2a) site at the center of the small $Si_{20}$ cages. For the other Ba vacancy on the Ba2 (6d) site at the center of the large $Si_{24}$ cages and for the Si vacancies in $Ba_8Si_{46}$, the reaction enthalpy increases, meaning that the vacancies are unstable. These results agree with the experimental observations of Ba vacancies in $Ba_8Si_{46}$. It was shown that the vacancies were indeed on the (2a) site

and that the superconducting temperature was decreased when the Ba vacancies increased after an annealing [19,43]. In the case of $Ba_{24}Si_{100}$, we always observe a reaction enthalpy larger than for the stoichiometric compound and therefore both Ba and Si vacancies should be unstable at ambient conditions. However, it will be interesting to see at their stability in temperature and in pressure. Indeed, a recent study shows in $Ba_{7.5}Si_{45}$ how Ba vacancies can be filled by host Si atoms at high pressure [19].

| Defect | a (Å) | $V_{at}$ (Å$^3$) | $V_{sc}-N_{sc}V_0/V_0$ | $H_{form}$ (eV/at) | $H_{react}$ (eV/at) |
|---|---|---|---|---|---|
| Pure $Ba_{24}Si_{100}$ | 14.164 | 22.916 | | -0.1845 | 0.024 |
| Vacancy Ba1 | 14.141 | 22.992 | 0.409 | -0.175 | 0.0264 |
| Vacancy Ba2 | 14.167 | 23.118 | 1.088 | -0.17 | 0.0315 |
| Vacancy Ba3 | 14.155 | 23.059 | 0.77 | -0.1725 | 0.0289 |
| Vacancy Si1 | 14.163 | 23.097 | 0.976 | -0.1824 | 0.0277 |
| Vacancy Si2 | 14.176 | 23.163 | 1.327 | -0.1829 | 0.0273 |
| Vacancy Si3 | 14.182 | 23.193 | 1.489 | -0.1789 | 0.0312 |
| Vacancy Si4 | 14.177 | 23.166 | 1.346 | -0.1836 | 0.0266 |
| Vacancy Si5 | 14.162 | 23.093 | 0.953 | -0.18 | 0.0302 |
| Vacancy Si6 | 14.195 | 23.252 | 1.808 | -0.1792 | 0.0309 |

**Table 4**: Lattice parameters, atomic volume $V_{at}$, formation enthalpies $H_{form}$, reaction enthalpies vs $BaSi_2$ and Si, $H_{react}$ of pure and vacancy containing type IX clathrate.

| Defect | a (Å) | $V_{at}$ (Å$^3$) | $V_{sc}-N_{sc}V_0/V_0$ | $H_{form}$ (eV/at) | $H_{react}$ (eV/at) |
|---|---|---|---|---|---|
| Pure $Ba_8Si_{46}$ | 10.3946 | 20.798 | | -0.1072 | 0.0524 |
| Vacancy Ba1 | 10.3503 | 21.076 | 0.708 | -0.0978 | 0.0445 |
| 2 vacancies Ba1 | 10.3066 | 21.054 | 0.639 | -0.0864 | 0.0379 |
| Vacancy Ba2 | 10.3758 | 20.921 | 0.312 | -0.0796 | 0.0626 |
| Vacancy Si1 | 10.4013 | 21.232 | 1.105 | -0.1089 | 0.0537 |
| Vacancy Si2 | 10.3469 | 20.9 | 0.26 | -0.0986 | 0.064 |
| Vacancy Si3 | 10.4068 | 21.266 | 1.19 | -0.1062 | 0.056 |

**Table 5**: Lattice parameters, atomic volume $V_{at}$, formation enthalpies $H_{form}$, reaction enthalpies vs $BaSi_2$ and Si, $H_{react}$ of pure and vacancy containing type I clathrate.

The bulk moduli are also reported in Tables 1-3 and decrease with the material densities (i. e. with increasing atom volume), which is the usual expected trend. Empty type I and II clathrates have the same bulk moduli, as observed previously [44], and similar bulk modulus as the orthorhombic $Si_{24}$. whereas the bulk modulus of type VIII clathrate is slightly larger and the bulk modulus of $Si_{100}$ is much smaller, as expected from its lower density. We note that recent experiments confirm that $Si_{24}$ has almost the same bulk modulus (86-91 GPa) [46] than type II $Si_{36}$ clathrate (90 GPa) [40-42]. When Ba is intercalated in the cages/tunnels, the bulk moduli decrease by less than 5 % type I and II clathrates and orthorhombic $M_4Si_{24}$, whereas it decreases by more than 15 % in type VIII clathrate. In contrast, the bulk modulus of the type IX clathrate increases by almost 50 % with Ba intercalation, confirming the stabilizing effect of the guest atom in this structure. We note that dB/dP increases significantly when Ba are intercalated, meaning that the filled structures have larger anharmonicity than the empty structure. When comparing our results with experiments, one can see that the theoretical values for diamond and type II clathrate are lower by about 10 % and 15 %, respectively. Our results for diamond are in good agreement with typical calculations with PBE exchange-correlation functional [51]. It was found a better agreement between experiments and LDA calculations in ref. 44. This is because we have used a GGA exchange-correlation functional which overestimates the lattice parameters and therefore underestimates the density compared to the experiments. Our calculations strongly underestimate the bulk modulus of type I $Ba_8Si_{46}$ but the agreement between calculations and experiments is reasonable for type IX $Ba_{24}Si_{100}$.

We have also calculated the electronic structure of the different empty and Ba-filled clathrate phases (see details in the SI). We find that all the Ba-filled phases are metallic whereas all the empty phases are semiconducting with a bandgap more than two times larger than that of diamond Si, except for $Si_{100}$ and orthorhombic $Si_{24}$, which have the same order of magnitude. When the empty semiconducting clathrates are filled by Ba atoms, this leads to a large upshift of the Fermi level in the conduction band, hence their metallic character, and this also reduces significantly the bandgap width by about 30-40 %. In the case of the orthorhombic $Ba_4Si_{24}$, the bandgap disappears.

## 4. Experimental results

### *4.1. Exploration of the P-T existence domain of $Ba_{24}Si_{100}$*

The first synthesis of $Ba_{24}Si_{100}$ at 1.5 GPa and 800 °C was reported in the early work of Yamanaka et al [15]. In a previous study, we obtained $Ba_8Si_{46}$ in similar conditions and $Ba_{24}Si_{100}$ only at lower pressure and temperature (1.1-1.3 GPa and 650-700 °C) [21]. Giving these contradictions and the prediction from first principles calculations that $Ba_8Si_{46}$ must be obtained instead of $Ba_{24}Si_{100}$ when the temperature is too high, we have scanned the P-T diagram between 0 and 2 GPa and up to 850 °C for the stoichiometry Ba:Si of 24:100 (see Figure 5).
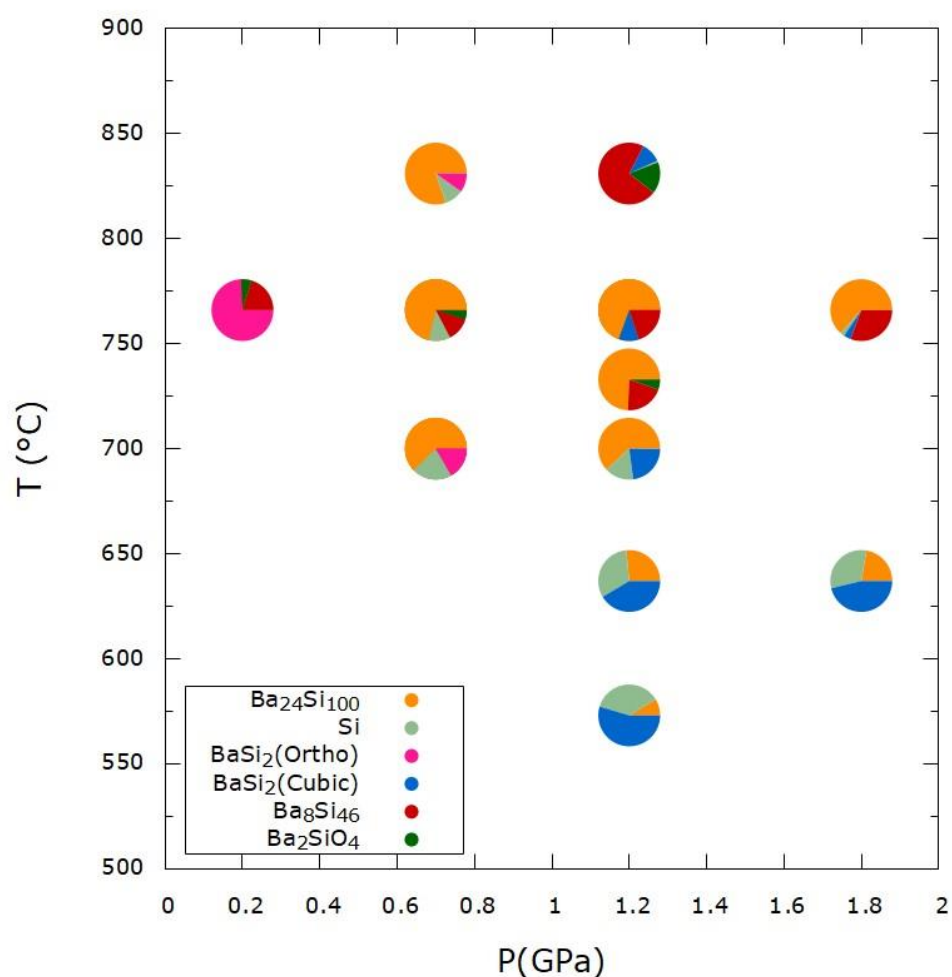


**Figure 5**: Ex-situ P-T phase diagram of $Ba_{24}Si_{100}$ synthesized under high pressure and high temperature conditions using a Belt apparatus. The different phases are given in mass fraction as obtained from Rietveld refinement.

We have seen in our ex-situ analysis that $Ba_{24}Si_{100}$ can form from 0.7 GPa up to 1.8 GPa and at least above 550 °C. However, it is not easy to get high purity type IX $Ba_{24}Si_{100}$ which is relatively more abundant than its secondary phases at lower pressure around 1.0 GPa. At 850°C and above 1 GPa, the type I $Ba_8Si_{46}$ becomes dominant and, at lower pressure, the orthorhombic $BaSi_2$ remains the most stable. When the pressure is decreased below 1 GPa, $Ba_8Si_{46}$ did not form at high temperature and we find $Ba_{24}Si_{100}$ with Si and orthorhombic $BaSi_2$ as secondary phases. Previously, it was observed by Yamanaka and Fukuoka [20] and confirmed by Toulemonde et al [21] that $Ba_8Si_{46}$ can form for P ≥ 2 GPa and at least up to 5 GPa. However, Toulemonde et al [21] also showed that $Ba_8Si_{46}$ can form at lower pressure (P = 1.5 GPa) at T = 800 °C. In our work, we confirm that $Ba_8Si_{46}$ can form at even lower pressure (P = 1.2 GPa) for T ≥ 800 °C. Thus the P-T domain existence of $Ba_8Si_{46}$ is much larger than the P-T domain existence of $Ba_{24}Si_{100}$. We also note that cubic $BaSi_2$ becomes more stable than orthorhombic $BaSi_2$ above 1 GPa and above 550 °C. This low pressure agrees with lower pressure boundary found by Evers [36] for the formation of the cubic $BaSi_2$ and this low temperature is close to the lower temperature boundary found by Imai and Kikegawa [37] in this pressure range for the formation of the cubic $BaSi_2$.

We have done a kind of ex-situ isobaric line on this P-T diagram at 1.2 GPa to better understand the reactivity pattern that leads to the formation of this type IX clathrate. For that, we have started from a mixture of Si and orthorhombic $BaSi_2$ using the stoichiometry of $Ba_{24}Si_{100}$ and used our high pressure-high temperature apparatus (see method). Synthesis done at 1.2 GPa and for a temperature of 550 °C results mostly to cubic $BaSi_2$ and Si, $Ba_{24}Si_{100}$ appears as secondary phase. $Ba_{24}Si_{100}$ is the dominant phase in the temperature range 725 °C – 800 °C above which $Ba_8Si_{46}$ is the main phase. Our experimental results agree with our first principles calculations although in this last case the pressure (1.5 GPa) and the temperature (1000°C) above which $Ba_8Si_{46}$ stabilizes were slightly larger.

## 4.2. In-situ study of the formation of $Ba_{24}Si_{100}$ under HP-HT

The formation of $Ba_{24}Si_{100}$ has been studied by in-situ isobar synchrotron XRD experiment for a pressure of 1 GPa. The powder patterns at different temperatures are shown in the Figure 7. The starting powder is a mixture of orthorhombic $BaSi_2$ and Si in the proportion of $Ba_{24}Si_{100}$ (diffraction pattern recorded at 20°C and 0 GPa). Our in-situ experiments show first the transformation of the orthorhombic $BaSi_2$ into the cubic $BaSi_2$ phase at temperature as low as 550 °C and then only after there is a reaction between the cubic $BaSi_2$ phase and the diamond Si phase for forming $Ba_{24}Si_{100}$. The $Ba_{24}Si_{100}$ clathrate appears in the temperature range between 698 °C and 765 °C with cubic $BaSi_2$ as traces. The phase $Ba_8Si_{46}$ appears only for temperature higher than 860 °C, which agrees with our ex-situ P-T study (see Figure 6). The in-situ study shows the appearance of the cubic $BaSi_2$ phase prior to the formation of $Ba_{24}Si_{100}$.
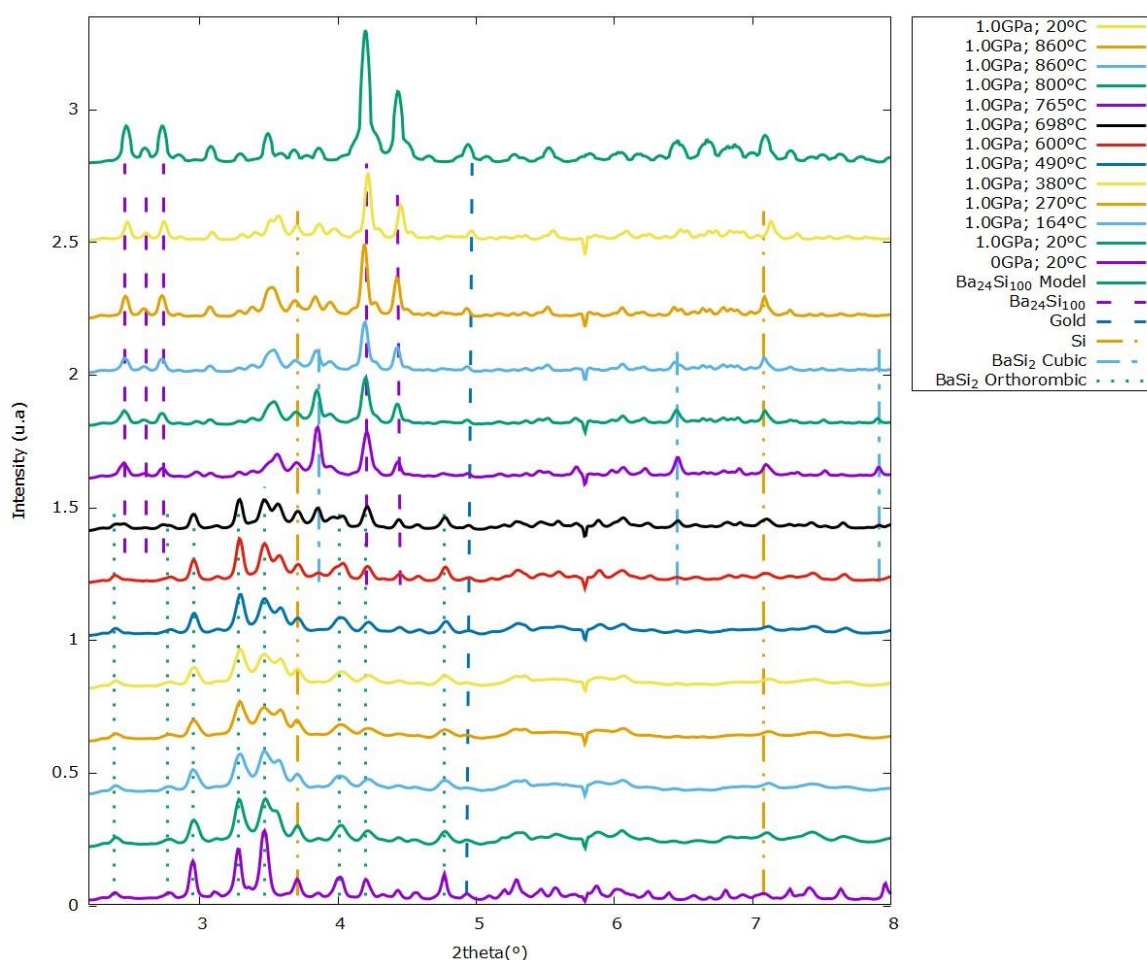


**Figure 6**: High pressure and high temperature experiment conducted at ESRF synchrotron on ID27 beam line.

### 4.3. Thermal stability of $Ba_8Si_{46}$ and $Ba_{24}Si_{100}$ at atmospheric pressure

The thermal stability of $Ba_8Si_{46}$ and $Ba_{24}Si_{100}$ was studied in Ar atmosphere from DTA/TGA experiments. Figure 7 shows the evolution of $Ba_8Si_{46}$ and $Ba_{24}Si_{100}$ in Ar atmosphere during heating up to 1000°C and cooling to room temperature. Three exothermic peaks are observed for $Ba_8Si_{46}$ during heating at 609°C, 646°C and 760°C (see Figure 7, left). XRD experiments performed after the DTA cycle showed the decomposition of $Ba_8Si_{46}$ into stable orthorhombic $BaSi_2$ and Si. The first peak in the DTA experiment at 609°C is attributed to the decomposition of metastable $Ba_8Si_{46}$ into stable $BaSi_2$ and Si. This $Ba_8Si_{46}$ decomposition was previously observed by Castillo *et al.* at 611°C for sample with stoichiometry $Ba_7Si_{46}$ [27]. The other thermal events at 646°C and 760°C could not be identified. Thermal analyses of $Ba_{24}Si_{100}$ show three exothermic peaks of low intensities at 504°C, 564°C and 687°C. XRD experiments after the DTA cycle showed the total decomposition of $Ba_{24}Si_{100}$ into stable orthorhombic $BaSi_2$ and Si. The first thermal event at 504°C is associated with the decomposition of cubic $BaSi_2$ to orthorhombic $BaSi_2$, initially present as a secondary phase in the sample. Indeed, Evers reported that the decomposition of cubic $BaSi_2$ into orthorhombic $BaSi_2$ started at 490°C [36]. The other thermal events in the DTA experiment can be related to the thermal decomposition of $Ba_{24}Si_{100}$. As a conclusion, this study performed under Ar atmosphere shows that $Ba_{24}Si_{100}$ is stable (without any phase change) up to about 560°C whereas $Ba_8Si_{46}$ is stable up to 600°C (for a heating rate of 5°C/min).
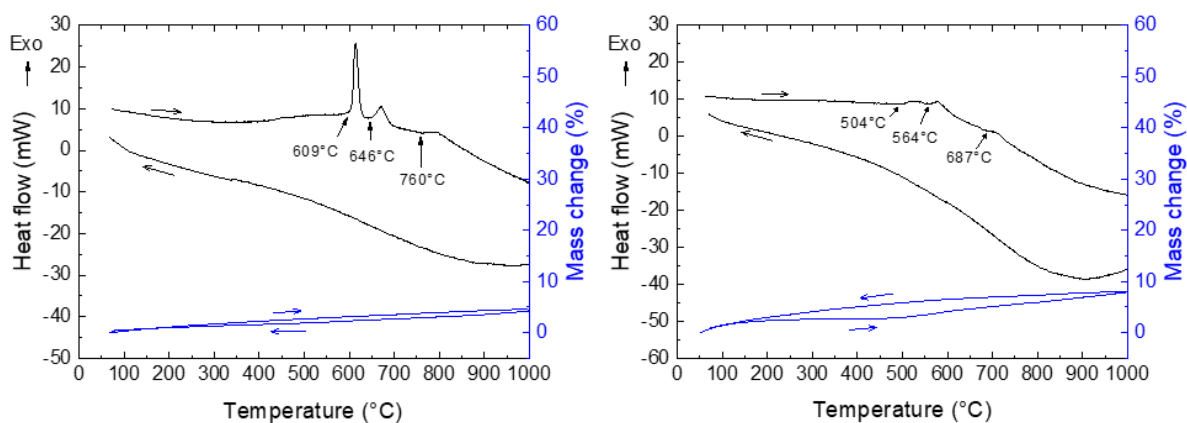


**Figure 7:** Thermal variation of the heat flow and sample mass of $Ba_8Si_{46}$ (left) and $Ba_{24}Si_{100}$ (right) under Ar atmosphere

Then we were interested in the effect of an oxidizing atmosphere on the evolution of $Ba_8Si_{46}$ and

$Ba_{24}Si_{100}$ with temperature. The DTA curves are reported in Figure 8. For $Ba_8Si_{46}$ three exothermic peaks

are observed during heating at 605°C, 698°C and 794°C (see Figure 8, left). The first peak observed at

605°C for $Ba_8Si_{46}$ is attributed to the decomposition of metastable $Ba_8Si_{46}$ into stable $BaSi_2$ and Si as

previously reported in Ar atmosphere. The two other thermal events at 698°C and 794°C are associated

with a high mass increase which suggests the formation of oxides. This was confirmed by XRD

experiments performed after the DTA cycle. XRD patterns show that the material is made of Si and

$Ba_2SiO_4$ (PDF 04-011-2153), $BaSiO_3$ (PDF 01-070-2112), $Ba_2Si_3O_8$ (PDF 04-012-8807), $BaSi_2O_5$ (04-

009-1824) and $Ba_5Si_8O_{21}$ (PDF 00-035-0766) oxides. These results suggest the decomposition of $Ba_8Si_{46}$

into stable $BaSi_2$ and Si from 605°C and the further oxidation of $BaSi_2$ from 698°C.



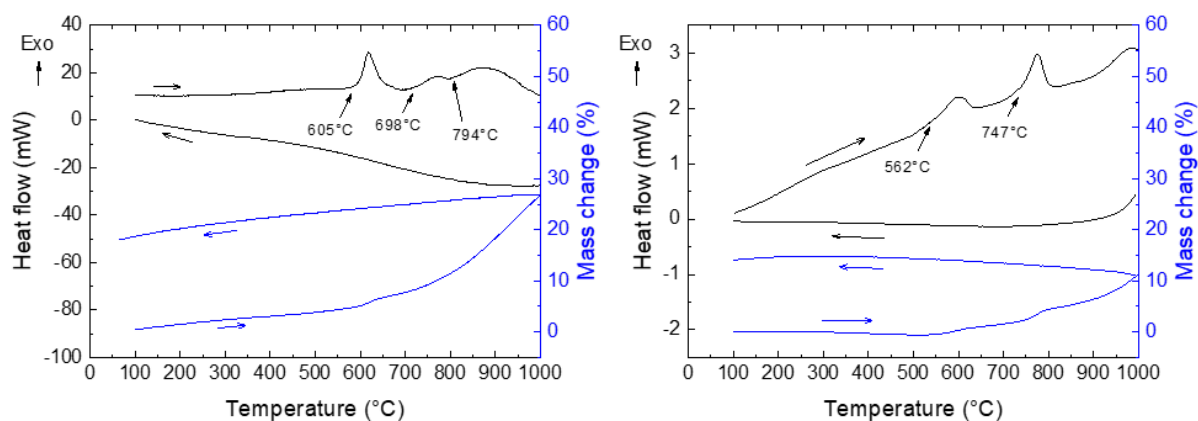**Figure 8:** Thermal variation of the heat flow and sample mass of $Ba_8Si_{46}$ (left) and $Ba_{24}Si_{100}$ (right)

under air

Considering $Ba_{24}Si_{100}$ (see Figure 8, right), two exothermic peaks are observed at 562°C and 747°C.

These thermal events are associated with a mass increase suggesting the formation of oxides. Ex-situ X-

ray diffraction patterns have been performed at different temperatures of the DTA cycle : 535°C, 670°C

(just before the two thermal events) and 1000°C (end of the thermal cycle) (see Figure 9). At 535°C,

there is no significant change of the XRD pattern in comparison with the as-synthesized sample,

meaning that $Ba_{24}Si_{100}$ is stable at least up to this temperature under oxidizing atmosphere. The XRD

pattern of the sample heated up to 670°C reveals a significant increase of diamond Si as well as an

increase of $BaSi_2$ and $Ba_2SiO_4$, compared to the as synthesized sample. Therefore, the first DTA thermal event at 562°C corresponds to the initiation of the decomposition of $Ba_{24}Si_{100}$ into Si and orthorhombic $BaSi_2$ as well as into $Ba_2SiO_4$, as confirmed by the concomitant mass increase. The present result confirms that the second DTA thermal event observed at 564°C in the DTA experiment under Ar (see Figure 7 (right)) must also correspond to the initiation of the decomposition of $Ba_{24}Si_{100}$ into Si and orthorhombic $BaSi_2$. The second thermal event at 747°C in the DTA experiment under air is associated with the formation of other oxides as suggested by the mass increase. The XRD pattern performed after the full DTA/TGA experiment (up to 1000°C) confirms the formation of $Ba_2Si_3O_8$ oxide and $BaSi_2O_8$ oxide richer in oxygen than $Ba_2SiO_4$. $Ba_2SiO_4$ oxide remains also present in very large amounts as well as diamond Si.
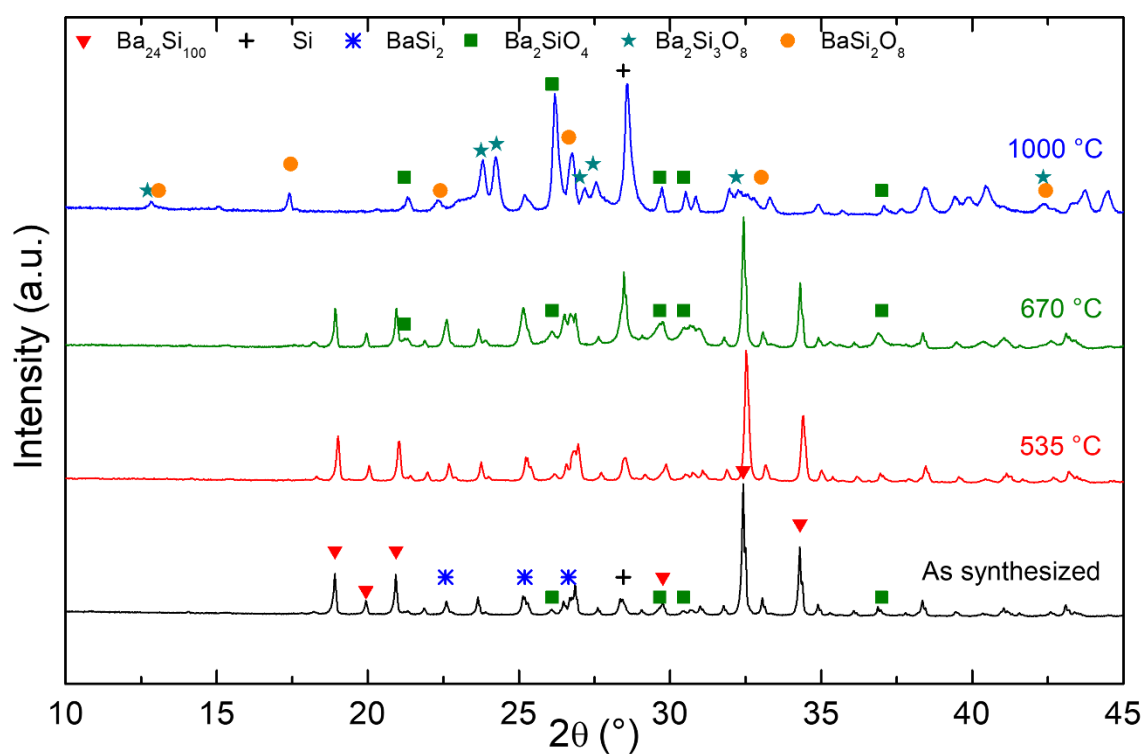


**Figure 9:** Ex-situ XRD patterns of $Ba_{24}Si_{100}$ at different temperatures.

This study shows that $Ba_{24}Si_{100}$ is stable (without any phase change) up to about 560°C whereas $Ba_8Si_{46}$ is stable up to 600°C in air similarly as in Ar atmosphere, oxidation occurring in a higher temperature range. We have also studied the effect of a thermal treatment under secondary vacuum on nanostructured powders of $Ba_{24}Si_{100}$ obtained from mechanical alloying as described by Moll *et al.* [29]. After a thermal treatment at 700°C during 4 days a complete decomposition of $Ba_{24}Si_{100}$ is observed whereas a thermal treatment at 500°C during 7 days did not improve the crystallite size of the nanostructured powders of $Ba_{24}Si_{100}$ and induces an increase of the amount of orthorhombic $BaSi_2$.Therefore, we have submitted the $Ba_{24}Si_{100}$ nanostructured powders to an annealing time of 21 days at 450°C under secondary vacuum. We did not observe any significant changes in the XRD patterns. This means that the nanostructured powders of $Ba_{24}Si_{100}$ are quite thermally stable at 450°C.

### *4.4 Electrical and thermoelectric properties of $Ba_{24}Si_{100}$ obtained under HP-HT*

We report in Figure 10 the evolution of the electrical resistivity, $\rho$, and of the Seebeck coefficient, $\alpha$, of $Ba_{24}Si_{100}$ in function of the temperature. The behavior is typical of metallic compounds. We find values of the electrical resistivity significantly lower than Lortz et al [24]. This should be due to higher density of the sample. The Seebeck coefficient is negative, corresponding to n-type material, in agreement with the electronic structure obtained from the DFT calculations (see supplementary information). The value of the Seebeck coefficient of $Ba_{24}Si_{100}$ at room temperature is 50 % larger in absolute value than the value found for $Ba_8Si_{46}$ by Castillo et al [27] but twice smaller in absolute value than the value found for $Ba_{24}Ge_{100}$ by Paschen et al [52]. The power factor $\alpha^2/\rho$ is very small (1 µW/m.K$^2$ at 250°C). In order to improve the thermoelectric properties of $Ba_{24}Si_{100}$, it would be necessary to move the Fermi level by about -0.6 eV within the bandgap observed in the electronic DOS of $Ba_{24}Si_{100}$ (see supplementary information). This would correspond to remove 16 electrons in $Ba_{24}Si_{100}$. This could be obtained by substituting Si by 16 atoms of Al, Ga or In in $Ba_{24}Si_{100}$. Similar substitution has been performed in $Ba_{24}Ge_{100}$ permitting to reach a very high figure of merit ZT of about 1.3 at 650°C for $Ba_{24}Ge_{85}Ga_{15}$ [53].
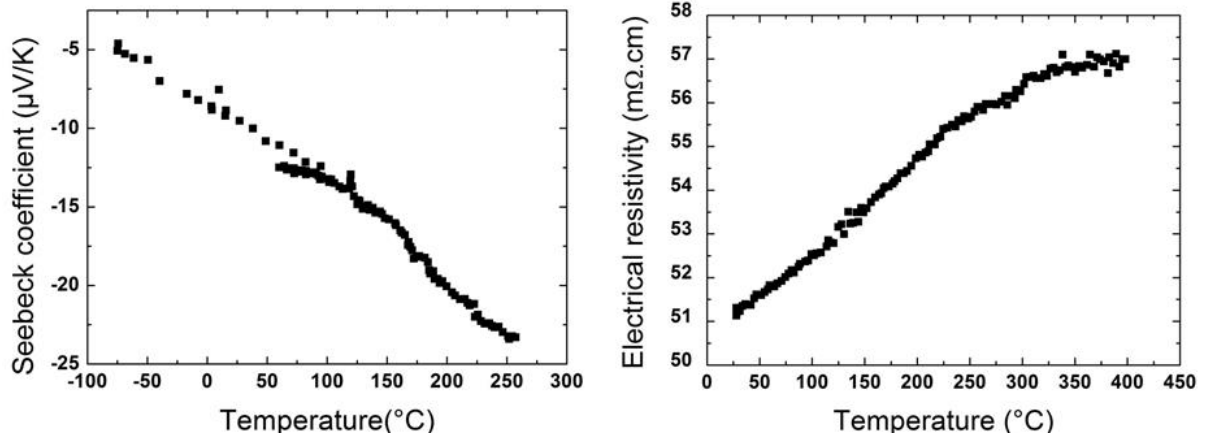
**Figure 10:** Thermal variation of the Seebeck coefficient and electrical resistivity of $Ba_{24}Si_{100}$

It was not possible to measure thermal conductivity in our samples. However, it is interesting to give an estimate of its value in the context of recent fundamental advances in the understanding of the thermal conductivity of complex crystals, i.e. crystal with a complex crystallographic unit cell [54,55]. Indeed, it has recently been shown that complexity leads to a separation of the phonon spectrum into an optical continuum made up of a high density of modes associated with the complexity of the structures (the 3N degrees of freedom) which dominate the specific heat ($C_v \sim 3NR$) and an acoustic part limited to just the three acoustic branches which dominate the lattice thermal conductivity. These two parts of the phonon spectrum are separated in energy at an energy threshold $\hbar\omega_{op}$ corresponding to the energy of the lowest energy optical mode. Ikeda et al have shown phenomenologically that the lattice thermal conductivity scales with this energy $\hbar\omega_{op}$ (or corresponding temperature $\theta_{op} = \hbar\omega_{op}/k_B$) [54]. Using the approximation of the relaxation time of the transport Boltzmann equation, Pailhès et al. showed that the propagated conduction associated with acoustic branches whose dispersions are limited by $\omega_{op}$ reads as [55]:

$$\kappa\left(T \gg \theta_{op}\right) = \frac{k_B}{6\pi^2} \frac{\omega_{op}^3}{v_s^2} l$$

With $v_s$ being the average sound velocity and $l$ the average mean free path.

Whereas the energy threshold $\hbar\omega_{op}$ is of about 5 and 7 meV in the type-I Ge and Si-clathrate respectively [56,57], in the case of $Ba_{24}Si_{100}$, we measure this threshold at an energy of 2.5 meV in a previous work [58]. The result is a reduction in the phase space in energy and wave-vectors available for acoustic phonon

states, which necessarily reduces the thermal conduction associated with these propagative states. Assuming a lower limit of the mean free path of about 20 nm, as observed in the clathrate $Ba_{7.81}Ge_{40.67}Au_{5.33}$ [57], and using $v_s = 3895$ m/s obtained from the Debye temperature determined from low temperature heat capacity experiments on $Ba_{24}Si_{100}$ by Rachi et al [23], we use this formula to estimate an upper limit for the thermal conductivity of 0.8 W/mK.

**Conclusion**

In the present paper, we have investigated the stability of different Ba-Si clathrates using DFT calculations and the stability of type I $Ba_8Si_{46}$ and type IX $Ba_{24}Si_{100}$ clathrates using calorimetry and diffraction experiments. The DFT calculations confirm that type IX $Ba_{24}Si_{100}$ clathrate is the most stable Ba-Si clathrate followed by type I $Ba_8Si_{46}$ clathrate and orthorhombic $BaSi_6$ and that pressure is the primary effect stabilizing these different phases. However, both the thermal vibrational and electronic contributions are of primary importance for stabilizing type IX $Ba_{24}Si_{100}$ clathrate against the ($BaSi_2$ + Si) mixture under 1-2 GPa pressure. We also find that Ba vacancies in the center of the small $Si_{20}$ cages increase the stability of type I clathrate whereas the Ba vacancies do not increase the stability of type IX clathrate. The presence of Ba in the cages of type IX clathrate increases significantly the stability and the mechanical properties of type IX clathrate, which is quite unstable when empty if it is compared to diamond Si and other empty Si clathrates. We have determined the P-T existence domain of type IX $Ba_{24}Si_{100}$ clathrate from ex-situ experiments, which was confirmed by in-situ synchrotron X-ray experiments. It extends from 0.7 to 1.8 GPa and between 650°C and 800°C and up to 875 °C between 0.7 and 1 GPa. At room pressure and under air atmosphere, the type IX $Ba_{24}Si_{100}$ clathrate is stable up to 560°C whereas the type I $Ba_8Si_{46}$ clathrate is stable up to 600°C. The thermoelectric properties of type IX $Ba_{24}Si_{100}$ clathrate are typical of a metallic compound, which means that it should be alloyed with atoms of the thirteenth column for improving its thermoelectric properties.

## Supplementary Information

Additional DFT details on crystal structure of the clathrates, equation of states of empty Si clathrates, formation energy Gibbs of $BaSi_2$ and electronic structure of clathrates ; example of XRD results for the in-situ study of P-T phase diagram of $Ba_{24}Si_{100}$. (PDF)

## Acknowledgements

## References

[1] Cros, C.; Pouchard, M. Sur les phases de type clathrate du silicium et des éléments apparentés (C, Ge, Sn): une approche historique. *C. R. Chimie* **2009**, *12*, 1014-1056.

[2] Nolas, G. S. *The Physics and Chemistry of Inorganic Clathrates*, Springer Series in Materials Science, Vol. 199, Dordrecht, 2014.

[3] Takabatake, T.; Suekuni, K.; Nakayama, T.; Kaneshita, E. Phonon-glass electron-crystal thermoelectric clathrates: experiments and theory. *Rev. Mod. Phys.* **2014**, *86*, 669-716.

[4] Claussen, W. F. Suggested structures of water in inert gas hydrates. *J. Chem. Phys*. **1951**, *19*, 259-260.

[5] v. Stackelberg, M.; Müller, H. R. On the structure of gas hydrates. *J. Chem. Phys.* **1951**, *19*, 1319-1320.

[6] Claussen, W. F. A second water structure of inert gas hydrates. *J. Chem. Phys.* **1951**, *19*, 1425-1426.

[7] Kamb, B. A clathrate crystalline form of silica. *Science* **1965,** *148*, 232-234.

[8] Kasper, J. S.; Hagenmuller, P.; Pouchard, M.; Cros, C. Clathrate structure of silicon $Na_8Si_{46}$ and $Na_xSi_{136}$ (x < 11). *Science* **1965**, *150*, 1713-1714.

[9] Eisenmann, B.; Schäfer, H.; Zagler, R. Die verbindungen $A^{II}_8B^{III}_{16}B^{IV}_{30}$ ($A^{II}$ = Sr, Ba; $B^{III}$ = Al, Ga; $B^{IV}$ = Si, Ge, Sn) und ihre käfigstrukturen. *J. Less-Comm. Met.* **1986**, *118*, 43-55.

[10] Kroner, R.; Nesper, R.; von Schnering, H. G. $Ba_6In_4Ge_{21}$, ein neuer Clathrat-typ. *Z. Kristallogr.* **1988**, *182*, 164-165.

[11] Zhao, J.-T.; Corbett, J. D. Zintl phases in alkali-metal-tin systems: $K_8Sn_{25}$ with condensed pentagonal dodecahedra of tin. Two $A_8Sn_{44}$ phases with a defect clathrate structure. *Inorg. Chem.* **1994**, *33*, 5721-5726.

[12] Fukuoka, H.; Iwai, K.; Yamanaka, S.; Abe, H.; Yoza, K.; Häming, L. Preparation and structure of a new germanium clathrate, $Ba_{24}Ge_{100}$. *J. Sol. State Chem.* **2000**, *151*, 117-121.

[13] Carillo-Cabrera, W.; Curda, J.; von Schnering, H. G.; Paschen, S.; Grin, Y. Crystal structure of hexabarium pentacosagermanide, $Ba_6Ge_{25}$. *Z. Kristallogr. NCS* **2000**, *215*, 207-208.

[14] Kim, S.-J.; Hu, S.; Uher, C.; Hogan, T.; Huang, B.; Corbett, J. D.; Kanatzidis, M. G. Structure and thermoelectric properties of $Ba_6Ge_{25-x}$ $Ba_6Ge_{23}Sn_2$, and $Ba_6Ge_{22}In_3$: Zintl phases with a chiral clathrate structure. *J. Solid State Chem.* **2000**, *153*, 321-329.

[15] Fukuoka H. and Yamanaka, S. High-pressure synthesis and structure of a new silicon clathrate $Ba_{24}Si_{100}$ *J. Organomet. Chem.* **2000**, *611*, 543-546.

[16] Yamanaka, S. and Maekawa, S. Structural evolution of the binary system Ba-Si under high pressure and high temperature. *Z. Naturforsch. b* **2006**, *61*, 1493-1499.

[17] Carillo-Cabrera, W.; Paschen, S.; Grin, Y. $EuGa_{2+x}Ge_{4-\pm x}$: preparation, crystal chemistry and properties. *J. Alloys Compds* **2002**, *333*, 4-12.

[18] Kim, D. Y.; Stefanoski, S.; Kurakevych, A.; Strobel, T. A. Synthesis ofn open-framework allotrope of silicon. *Nat. Mater.* **2015**, *14*, 169-173.

[19] Debord, R.; Euchner, H.; Pischedda, V.; Hanfland, M.; San Miguel, A.; Mélinon, P.; Pailhès, S.; Machon, D. Isostructural transition by point defect reorganization in the binary type-I clathrate $Ba_{7.5}Si_{45}$. *Acta Mater.* **2021**, *210*, 116824.

[20] Yamanaka, S.; Enishi, E.; Fukuoka, H.; Yasukawa, M. High-pressure synthesis of a new silicon clathrate superconductor $Ba_8Si_{46}$. *Inorg. Chem.* **2000**, *39*, 56-58.

[21] Toulemonde, P.; San Miguel, A.; Merlen, A.; Viennois, R.; Le Floch, S.; Adessi, Ch.; Blase, X.; Tholence, J. L. High pressure synthesis and properties of intercalated silicon clathrates. *J. Phys. Chem. Solids* **2006**, *67*, 1117-1121.

[22] Viennois, R.; Toulemonde, P.; Paulsen, C.; San Miguel, A. Superconductivity in the $Ba_{24}Si_{100}$ cubic clathrate with $sp^2$ and $sp^3$ silicon bondings. *J. Phys.: Cond. Mat.* **2005**, *17*, L311-L319.

[23] Rachi, T.; Yoshino, H.; Kumashiro, R. *et al.* Superconductivity and physical properties of $Ba_{24}Si_{100}$ determined from electric transport, specific-heat capacity, and magnetic susceptibility measurements. *Phys. Rev. B* **2005**, *72*, 144504.

[24] Lortz, R.; Viennois, R.; Petrovic, A.; Wang, Y.; Toulemonde, P.; Meingast, C.; Koza, M. M.; Mutka, H.; Bossak, A.; San Miguel, A. Phonon density of states, anharmonicity, electron-phonon coupling, and possible multigap superconductivity in the clathrate superconductors $Ba_8Si_{46}$ and $Ba_{24}Si_{100}$: factors behind large difference in $T_c$. *Phys. Rev. B* **2008**, *77*, 224507.

[25] Fukuoka, H.; Kiyoto, J.; Yamanaka, S. Synthesis and superconductivity of barium deficient type I silicon clathrate compound, $Ba_{8-x}Si_{46}$. *J. Phys. Chem. Solids* **2004**, *65*, 333-336.

[26] Imai, M.; Kikegawa, T. In situ observation of the formation of Si clathrate $Ba_8Si_{46}$ at high pressure and high temperature. *Inorg. Chem.* **2008**, 47, 8881-8883.

[27] Castillo, R.; Schnelle, W.; Bobnar, M.; Burkhardt, U.; Böhme, B.; Baitinger, M.; Schwarz, U.; Grin, Y. The clathrate $Ba_{8-x}Si_{46}$ revisited: preparation routes, electrical and thermal transport properties. *Z. Anorg. Allg. Chem.* **2015**, *641*, 206-213.

[28] Liang, Y.; Böhme, B.; Reibold, M.; Schnelle, W.; Schwarz, U.; Baitinger, M.; Lichte, H.; Grin, Y. Synthesis of the clathrate-I phase $Ba_{8-x}Si_{46}$ via redox reactions. *Inorg. Chem.* **2011**, *50*, 4523-4528.

[29] Moll, A.; Beaudhuin, M.; Legrand, V.; Debord, R.; Pailhès, S.; Viennois, R.; Fréty, N. Mechanical alloying as a new synthesis route for metastable silicon clathrate. *Mater. Lett.* **2017**, *187*, 1-3.

[30] Kresse, G.; Joubert, D., From ultrasoft pseudopotentials to the projector augmented-wave method. *Phys. Rev. B* **1999**, *59*, 1758-1775.

[31] Perdew, J. P.; Burke, K.; Erzenhof, M., Generalized gradient approximation made simple. *Phys. Rev. Lett.* **1996**, *77*, 3865-3868.

[32] Birch, F. Finite elastic strain of cubic crystals. *Phys. Rev.* **1947**, *71*, 809-824.

[33] Colinet, C.; Viennois, R.; Tedenac, J.-C. First principles study of the structural stability of intermetallic compounds in the Si-Zr system. *Calphad* **2012**, *36*, 118-126.

[34] Imai, M. Thermal expansion of alkaline-earth-metal disilicides $AeSi_2$ (Ae = Ca, Sr, and Ba). *Jpn. J. Appl. Phys.* **2011**, *50*, 101801.

[35] For the thermal expansion of Ba, see https://www.webelements.com

[36] Evers, J. Transformation of three-connected silicon in $BaSi_2$. *J. Solid State Chem.* **1980**, *32*, 77-86.

[37] Imai, M.; Kikegawa, T. Phase transitions of alkaline-earth-metal disilicides $M_{AE}Si_2$ ($M_{AE}$ = Ca, Sr, and Ba) at high pressures and high temperatures. *Chem. Mater.* **2003**, *15*, 2543-2551.

[38] Toby, B. H.; von Dreele, R. B. GSAS-II:the genesis of a modern open-source all purpose crystallography software package *J. Appl. Cryst.* **2013**, *46*, 544-549.

[39] Rodriguez-Carvajal, J. Magnetic structure determination from powder diffraction using the program Fullprof. *Applied Crystal.* **2001**, 30-36.

[40] San Miguel, A.; Mélinon, P.; Connétable, D.; Blase, X.; Itié, J. P.; Polian, A.; Reny, E.; Cros, C.; Pouchard, M. High pressure behavior of silicon clathrates : a new class of low compressibility materials. *Phys. Rev. Lett.* **1999**, *83*, 5290-5293.

[41] Gryko, J.; McMillan, P. F.; Marzke, R. F.; Ramachadran, G. K.; Patton, D.; Deb, S. K.; Sankey, O. F. Low-density framework form of crystalline silicon with a wide optical band gap. *Phys. Rev. B* **2000**, *62*, R7707-R7710.

[42] Ramachandran, G. K.; McMillan, P. F.; Deb, M. Somayazulu, S. K.; Gryko, J.; Dong, J.; Sankey, O. F. High-pressure phase transformation of the silicon clathrate $Si_{136}$. *J. Phys.: Cond. Mat.* **2000**, *12*, 4013-4020.

[43] Fukuoka, H.; Kiyoto, J.; Yamanaka, S. Superconductivity of metal deficient silicon clathrate compounds, $Ba_{8-x}Si_{46}$. *Inorg. Chem.* **2003**, *42*, 2933-2937.

[44] San Miguel, A.; Mélinon, P.; Connétable, D.; Blase, X.; Tournus, F.; Reny, E.; Yamanaka, S.; Itié, J. P. Pressure stability and low compressibility of intercalated cagelike materials: the case of silicon clathrates. *Phys. Rev. B* **2002**, *65*, 054109.

[45] Toulemonde, P.; Machon, D.; San Miguel, A.; Amboage, M. High pressure x-ray diffraction study of the volume collapse in $Ba_{24}Si_{100}$ clathrate. *Phys. Rev. B* **2011**, *83*, 134110.

[46] Shiell, T. B.; Strobel, T. A. Compression of sodium-filled and empty open-framework $Si_{24}$ under quasihydrostatic and nonhydrostatic conditions. *Phys. Rev. B* **2020**, *102*, 094107.

[47] Norouzzadeh, P.; Myles, C. W.; Vashae, D. Phonon dynamics in type-VIII silicon clathrates: beyond the rattler concept. *Phys. Rev. B* **2017**, *95*, 195206.

[48] Amsler, M.; Botti, S.; Marques, M. A. L.; Lenosky, T. J.; Goedecker, S. Low-density silicon allotropes for photovoltaic applications. *Phys. Rev. B* **2015**, *92*, 014101.

[49] Ceirqueira, T. F. T.; Pailhès, S.; Debord, R.; Giordano, V. M.; Viennois, R.; Shi, J.; Botti, S.; Marques, M. A. L. Prediction and synthesis of a non-Zintl silicon clathrate. *Chem. Mater.* **2016**, *28*, 3711-3717.

[50] Imai, Y.; Watanabe, A. Energetic evaluation of Ba- and Sr-Si clathrate formation at high pressures by first-principle pseudopotential calculations. *Intermet.* **2010**, *18*, 542-547.

[51] Lejaeghere, K.; Bihlmayer, G.; Björkman, T. *et al.*, Reproducibility in density functional theory calculations of solids. *Science* **2016**, *351*, aad3000.

[52] Paschen, S.; Tran, V. H.; Baenitz, M.; Carillo-Cabrera, W.; Grin, Y.; Steglich, F. Clathrate $Ba_6Ge_{25}$: thermodynamic, magnetic, and transport properties. *Phys. Rev. B* **2002**, *65*, 134435.

[53] Kim, J.-H.; Okamoto, N. L.; Kishida, K.; Tanaka, K.; Inui, H. High thermoelectric performance of type-III clathrate compounds of the Ba-Ge-Ga system. *Acta Mater.* **2006**, *54*, 2057-2062.

[54] Ikeda, M. S.; Euchner, H.; Yan, X.; Tomes, P.; Prokofiev, A.; Prochaska, L.; Lientschnig, G.; Svagera, R; Hartmann, S.; Gati, E.; Lang, M.; Paschen, S. Kondo-like phonon scattering in thermoelectric clathrates. *Nat. Commun.* **2019**, *10*, 887.

[55] Pailhès, S.; Giordano, V. M.; Turner, S. R.; Lory, P.-F.; Candolfi, C.; de Boissieu, M.; Euchner, H. From phonons to the thermal properties of complex thermoelectric crystals: the case of type-I clathrates. *Res. Phys.* **2023**, *49*, 106487.

[56] Pailhès, S.; Euchner, H.; Giordano, V. M.; Debord, R.; Assy, A.; Gomès, S.; Bosak, A.; Machon, D.; Paschen, S.; de Boissieu, M. Localization of propagative phonons in a perfectly crystalline solid. *Phys. Rev. Lett.* **2014**, *113* 025506.

[57] Lory, P.-F.; Pailhès, S.; Giordano, V. M. *et al* Direct measurement of individual phonon lifetimes in the clathrate compound $Ba_{7.81}Ge_{40.67}Au_{5.33}$. *Nat. Commun.* **2017**, *8*, 491.

[58] Viennois, R.; Koza, M. M.; Debord, R.; Toulemonde, P.; Mutka, H.; Pailhès, S. Anisotropic low-energy vibrational modes as an effect of the cage geometry in the binary barium silicon clathrate $Ba_{24}Si_{100}$. *Phys. Rev. B* **2020**, *101*, 224302.